

# Investigation of the June 21 and 25, 2015 CMEs using EUHFORIA

Somaiyh Sabri<sup>1</sup> and Stefaan Poedts<sup>2,3</sup>

<sup>1</sup>Institute of Geophysics, Faculty of Physics, University of Tehran, Tehran, Iran

<sup>2</sup>Center for mathematical Plasma Astrophysics, Department of Mathematics, KU Leuven, Celestijnenlaan 200B, 3001 Leuven, Belgium

<sup>3</sup>Institute of Physics, University of Maria Curie-Skłodowska, ul. Radziszewskiego 10, PL-20-031 Lublin, Poland

**Correspondence:** Somaiyh Sabri (s.sabri@ut.ac.ir)

**Abstract.** In this research, the EUropean Heliosphere FORecasting Information Asset (EUHFORIA) is used as a mathematical model to examine how coronal mass ejections (CMEs) move through and interact with the background solar wind flow, taking into account three dimensions and changes over time. Magnetohydrodynamic (MHD) simulations were conducted to analyse the propagation patterns of two specific CMEs on June 21 and 25, 2015, respectively. The EUHFORIA simulations for the inner region of the heliosphere involve incorporating initial conditions related to the CMEs and the background solar wind using photospheric magnetograms as boundary conditions. Comparative examination using WIND spacecraft data and OMNI **web data service** reveals that the EUHFORIA model offers a moderately precise depiction. **The research emphasizes that the interactions of CMEs are crucial in shaping their effects on Earth, indicating that their initial speeds, while comparable, have a lesser impact.** Besides, the EUHFORIA numerical model aligns with the findings of the GFZ German research centre; this implies that EUHFORIA can also compute and potentially forecast the impact of CMEs on the Earth.

## 1 Introduction

Space weather refers to the impact of solar activity on Earth and other celestial bodies in the solar system. The scientific community recognizes the increasing significance of studying space weather due to its impact on human activities. Various environments require distinct principles of physics to be utilized. To address this, the ESA Virtual Space Weather Modelling Center (VSWMC) has expanded its capabilities to allow the integration of a series of models for forecasting (Poedts et al. , 2020). The current model for developing heliospheric wind and CMEs, such as the coronal model in EUHFORIA, relies on the Wang-Sheeley-Arge (WSA) model (Arge et al. , 2003). It is important to highlight that alternative coronal models like multi-VP need more CPU time (Reville et al. , 2015; Samara et al. , 2021).

The release of a significant amount of magnetic energy can occur when there are rapid changes in the magnetic structures through a process called magnetic reconnection (McLaughlin et al. , 2018; Sabri et al. , 2018, 2019, 2020a, b, 2021a, b, 2022, 2023; Kumar et al. , 2024). CMEs occur when a large quantity of plasma from the Sun's corona is expelled into space. They are explosive events on the Sun where plasma and magnetic fields are forcefully ejected and form significant structures. These structures,

along with their shocks, travel through the heliosphere. They are crucial in linking solar eruptions to the subsequent effects on  
25 interplanetary and geomagnetic disturbances (Dryer , 1994).

In general, the majority of fast reverse shocks are generated by interactions between slow and fast-stream regions. In contrast, fast-forward shocks are primarily caused by CMEs throughout all stages of solar activity except during periods of solar minimum (Kilpua et al. , 2015). Fast collisionless shocks are significant solar occurrences. The steepening of fast magnetoacoustic waves is connected to the sudden increase in both the magnetic field strength and the plasma parameters of the solar  
30 wind. This steepening process may be responsible for the creation of fast shocks. Studying the significance of fast shocks in solar-terrestrial physics is crucial as it accelerates charged particles to high energies (around tens of MeV). They pose significant risks to satellite technology and human ventures in space (Manchester et al. , 2005).

Since CMEs drive major geomagnetic storms, it is important to investigate their start and propagation to forecast their arrival  
35 at Earth, any planet, or satellite. Space weather forecasting depends on different factors, including the eruptions at the Sun and their moving from the solar corona to the planets or satellites in the inner heliosphere (Riley & Ben-Nun , 2021; Verbeke et al. , 2022). In this line, magnetohydrodynamic simulations help investigate the propagation of CMEs, studying their interactions with solar wind structures and also other CMEs and computing their geoeffectiveness.

40 Understanding three-dimensional background solar wind through numerical analysis is crucial for accurately predicting and studying space weather phenomena, specifically for identifying the specific behaviour of three-dimensional CME propagation. Successful combination of two-dimensional and three-dimensional MHD coronal and heliospheric models has been performed by Wu et al. (1999); Odstrcil et al. (2004). The coronal simulation began with an initial potential magnetic field and a spherically symmetric Parker solar wind (Odstrcil et al. , 2002). The coronal model utilized a series of MHD flow parameters over  
45 time, which served as a boundary condition for the heliospheric model.

Our study aims to investigate the propagation and interaction of specifically identified CMEs with other CMEs and the solar wind. In this research, we selected two CMEs and examined their propagation using 3D MHD modelling EUHFORIA. Our goal was to determine the timing of their arrival at Earth and assess whether they would cause geomagnetic storms.

## 50 **2 Physics of coronal mass ejections**

The occurrence of CMEs is typically connected to the disruption of a coronal magnetic structure that resembles a partially toroidal magnetic coil, which is anchored in two opposite polarities of the Sun's **magnetic field** on its surface (Torok & Kliem , 2005; Schmieder et al. , 2015; Green et al. , 2018). This explanation pertains to the requirement for the presence of magnetic energy and electric currents in the coronal structure for their acceleration into the corona and interplanetary space. Concerning  
55 the magnetic field configuration before an eruption, it is important to note that the cause of the eruption cannot solely be attributed to a flux rope. Other factors, such as a sheared arcade or multiple quadrupolar structures, could also lead to eruptions

Time at 21.5R	Longitude(deg)	Latitude(deg)	Half Angle(deg)	Speed(km/s)
2015-06-010T00:05:00Z	-31	30	43	853
2015-06-014T08:47:00Z	40	-23	36	701
2015-06-016T10:53:00Z	25	-50	39	570
2015-06-18T20:00:00Z	-50	11	45	1000
2015-06-19T14:59:00Z	9	-33	54	603
2015-06-21T05:01:00Z	-8	7	47	1250
2015-06-22T21:10:00Z	3	14	45	1155
2015-06-25T10:51:00Z	46	23	41	1450

**Table 1.** List of the CMEs and their characteristics

(Song et al. , 2014; Nindos et al. , 2020). It must be noted that the eruption is pioneered by swelling and slow increasing motion of the pre-eruptive structure (Bojan , 2021).

60 The reduced solar activity in cycle 24 increases the speed of CMEs. In this scenario, most CMEs manifest as halo CMEs (HCMEs), forming closer to the Sun. The Solwind coronagraph on the P78-1 spacecraft was the first to identify this type of CMEs (Howard et al. , 1985). Information gathered from the coronagraphs on the Solar and Heliospheric Observatory (SOHO) and the Solar Terrestrial Relations Observatory (STEREO) has revealed that halo CMEs are a type of CME that are generally fast and wide (Gopalswamy et al. , 2013; Makela et al. , 2016). The crucial matter is that the halos contain many highly energetic CME populations. Almost 58% of CMEs result in low-frequency type 2 radio bursts, while 67% of CMEs cause intense geomagnetic storms ( $DSt < -100nT$ ) and around 80% in CMEs related to the large solar energetic particle (SEP) events and 100% associated with gamma-ray emission (Gopalswamy et al. , 2018, 2019b).

70 To have a halo shape, CMEs must begin near the Sun's central meridian, either in the front or back, as distinguished from the coronagraph. Roughly 10% of halo CMEs originate from the limb, and these are particularly fast, with a speed of ( $1400kms^{-1}$ ) (Gopalswamy et al. , 2020; Cid et al. , 2012). There is a significant probability that a frontal halo CME observed from the line connecting the Sun and Earth will collide with the Earth and result in a geomagnetic storm (Zhao & webb , 2003; Scolini et al. , 2018). During solar cycle 24, the number of halo CMEs remained relatively stable despite a decline of over 40% in the sunspot number (SSN). This observation is supported by studies conducted by (Michalek et al. , 2019; Dagnew et al. , 2022). Another aspect to consider is that the reduced pressure in the heliosphere during Solar Cycle 24, as compared to Solar Cycle 23, led to the expansion of CMEs. These CMEs could be classified as halos, even if they originated from areas further away from the central meridian distance (CMD).

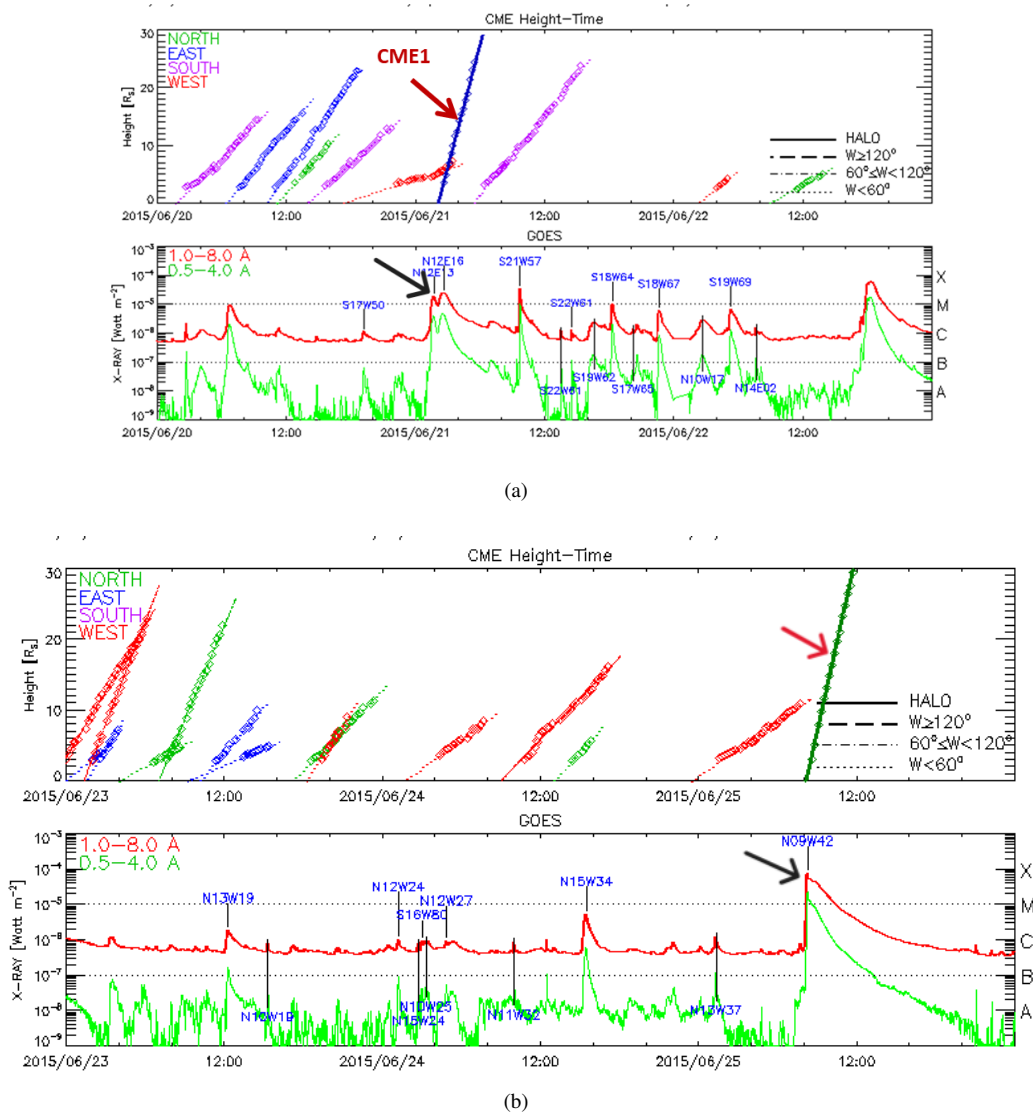


**Figure 1.** Overview of the early evolution and eruption of CME1 and CME2 that defined with red arrow. Panels (a) and (b) span June 20-25, 2015. Panel (a) illustrates the Height-time plot of CME1 and the M-class flare on June 21, 2015. Panel (b) depicts the Height-time plot of CME2 and the M-class flare on June 25, 2015. Flares indicated with a black arrow can be associated with the eruptions of CME1 and CME2 and the solar source coordinates of the flares are labelled in the GOES X-ray intensity plots.

Source: CDAW catalogue: [https://cdaw.gsfc.nasa.gov/CME\\_list/](https://cdaw.gsfc.nasa.gov/CME_list/)

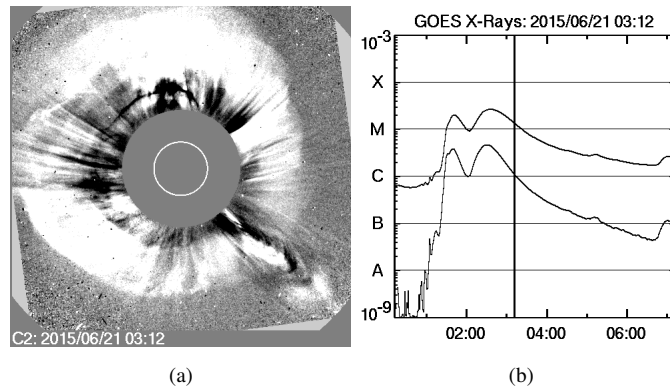


**Figure 2.** CME1 and flare development on June 21, 2015, in the LASCO C2 field of view and GOES X-ray, respectively. This figure is based on the SOHO LASCO CME CATALOG, accessed through the following link. [https://cdaw.gsfc.nasa.gov/CME\\_list/](https://cdaw.gsfc.nasa.gov/CME_list/)

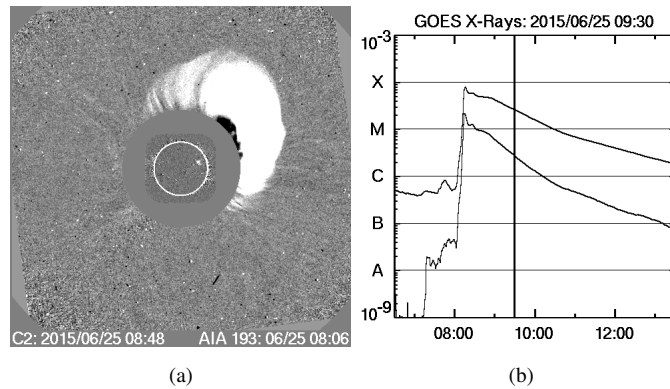


**Figure 3.** CME2 and flare generation on June 25, 2015, in the LASCO C2 field of view and GOES X-ray respectively. This figure is based on the SOHO LASCO CME CATALOG, which can be accessed through the following link. [https://cdaw.gsfc.nasa.gov/CME\\_list/](https://cdaw.gsfc.nasa.gov/CME_list/)

### 3 Observation of the 10-25 June 2015 CMEs

80 The analysis of a CME involves assessing its size, speed, and direction, which are critical parameters in understanding its behaviour. Space Weather Prediction Center (SWPC) forecasters use coronagraph imagery from orbital satellites to determine the probability of any potential impact on Earth based on specific characteristics. The Large Angle and Spectrometric Coronagraph (LASCO) is a coronagraph installed on the NASA Solar and Heliospheric Observatory (SOHO). This device has two capabilities for capturing images of the Sun's corona using optics. One range, called C2, can capture images within a distance range of 1.5 to 6 times the radius of the Sun, while the other range, called C3, can capture images within a distance range of 3 to 32 times the radius of the Sun. The LASCO instrument is forecasters' main tool to examine and classify CMEs. Nevertheless,

85

there is another coronagraph on the NASA STEREO-A spacecraft that serves as an extra resource.

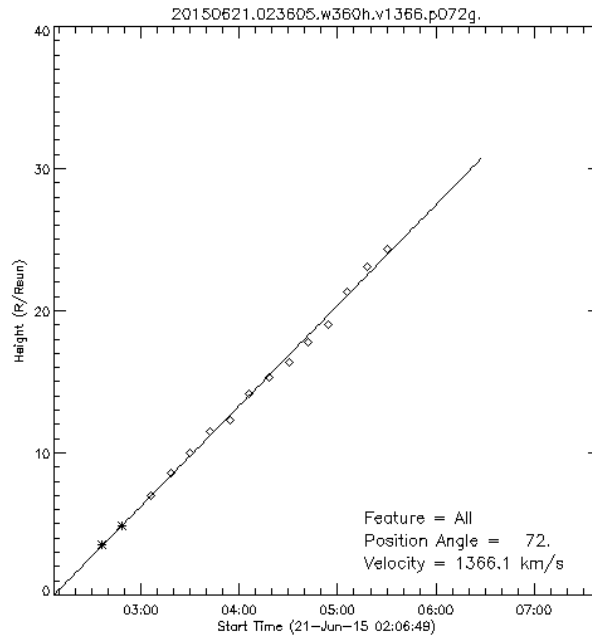
This portion examines the signs of two halo CMEs on June 21 and 25, 2015. Figs. 1 shows the occurrence of two halo coronal mass ejections. The initial CME occurred on 21 June 2015 at around 03:00 UT with velocity  $1366\text{km/s}$  and was associated with an M2.6 flare at N12E16. CME2 commenced on June 25, 2015, at 08:36 UT with a velocity of  $1627\text{ km/s}$  that linked to an M 7.9 flare, which was situated at N09w42. In each panel, the first image demonstrates the flares and X-ray intensities related to two CME eruptions. These eruptions were detected in the field of view of the C2 instrument of Large Angle and Spectrometric Coronagraph (LASCO) on the Solar and Heliospheric Observatory (SOHO) and also COR-2 instrument on board the Sun-Earth Connection Coronal and Heliospheric Investigation (SECCHI) on the twin-spacecraft STEREO (Brueckner et al. , 1995; Kaiser et al. , 2008).

In Figs. 2, CME1 was detected in the C2 FOV at 03:12 UT with the following M2.6 flare that is in agreement with the results in panel (a) of Fig. 1. Besides, panel (a) of Fig. 2 depicts that this CME could be considered as full halo CME. These types of CMEs usually take place in the area of the Sun with localized and strong magnetic fields, including active regions. Moreover, in Fig. 3, CME2 was also viewed in the C2 FOV at 08:06 UT with its following M 7.9 flare in according to the panel (b) of Fig. 1.

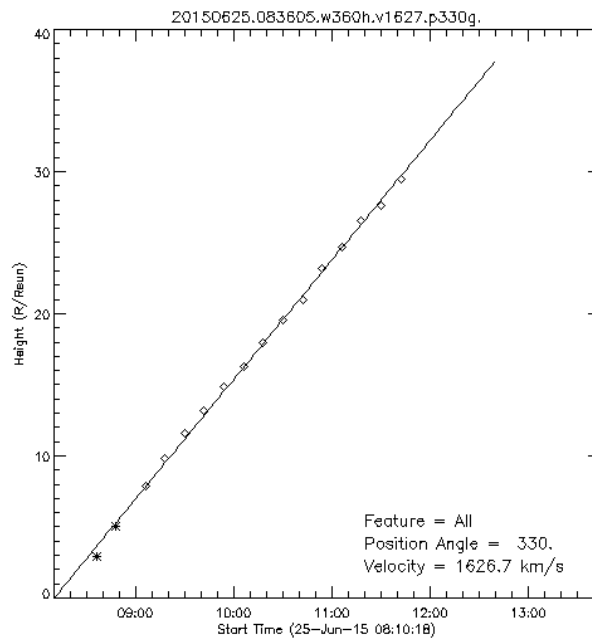
According to panel (a) of Fig. 4, CME1 that happened on 21 June 2015 has the linear fit speed  $1366\text{ km/s}$ . As we know, CMEs move outward from the Sun at speeds ranging from slower than  $250\text{km/s}$  to as fast as almost  $3000\text{km/s}$ . The fastest Earth-directed CMEs can arrive on our planet in around 15 – 18 hours. Then, this CME with speed  $1366\text{km/s}$  is a moderately fast CME and should arrive at Earth within one day. In the case of the second selected CME or CME2, it has the linear fit speed  $1626\text{km/s}$  then it is somehow faster than the first CME. It could be expected that CME2 may result in significant storms on the Earth.

More intense CMEs usually occur when magnetic field structures or flux ropes in the lower corona of the Sun, which are highly twisted, become disrupted and change their shape to a less tense configuration. This phenomenon is referred to as magnetic reconnection. This occurrence can be accompanied by the sudden release of electromagnetic energy in the form of a solar flare. As demonstrated in panel (b) of Figs. 2 and 3, these CMEs were accompanied by M-class solar flares.

Fig. 5 illustrates the distinct characteristics of the CMEs. The shocks caused by CMEs are represented by the red line in every panel. The shock is identified by the increase in both velocity and number density. The shock candidates were detected using a visual inspection technique. In this approach, we examined daily graphs of solar wind plasma and magnetic field characteristics to identify potential instances of shock. Simultaneous and abrupt changes in both plasma and magnetic field factors were considered. These jumps had to be considerable enough and fulfill the properties of either fast forward (FF) or fast reverse shock (FR).



(a)



(b)

**Figure 4.** CME speeds with linear fit and also second order fit for both two CMEs that happened on 21 June, 2015 and 25 June,2015. Panel (a) shows the linear fit velocity, and panel (b) demonstrates the second-order fit for the first CME, which happened on June 21, 2015. Panel (c) shows the linear fit and panel (d) defines the second order fit velocity for the second CME happed on 25 June,2015. This figure is based on the SOHO LASCO CME CATALOG, accessed through the following link. [https://cdaw.gsfc.nasa.gov/CME\\_list/](https://cdaw.gsfc.nasa.gov/CME_list/)

Fast shocks can be categorized into two types: fast forward shocks, which move in the opposite direction away from the Sun, and fast reverse shocks, which move towards the Sun while exhibiting a significant outflow of solar wind from the Sun. When fast-forward shocks pass over the spacecraft in the solar wind, there is a simultaneous rise in the magnetic field and all plasma parameters. This is depicted in Figs. 5. On the other hand, in the case of fast reverse shocks, the speed increases, but the density of the solar wind, magnetic field strength, and temperature all decrease. Compared to CME1, CME2, depicted in Figs. 5, has a substantial increase in velocity and magnetic field strength. This could potentially result in a severe storm. Furthermore, the notable values of  $N_p$  and  $T_p$  on the second panel for CME2, in contrast to CME1, also confirm the possibility that CME2 could result in a severe storm. This will be elaborated further in the subsequent discussion.

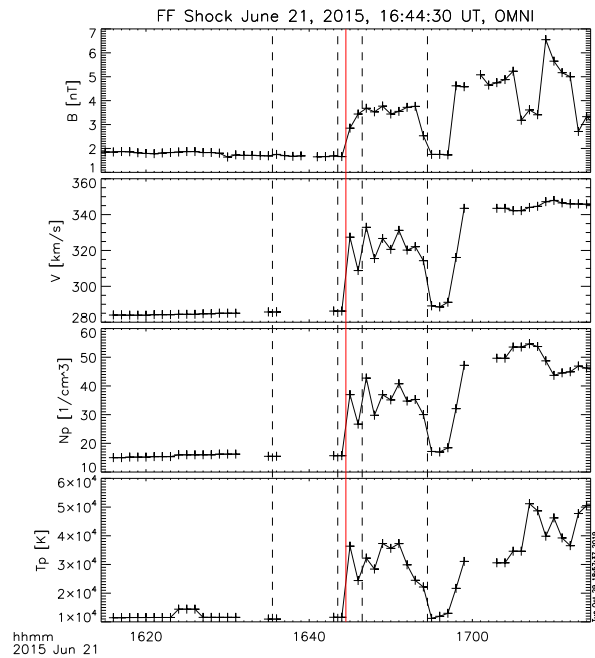
130

#### 4 Numerical results and discussion

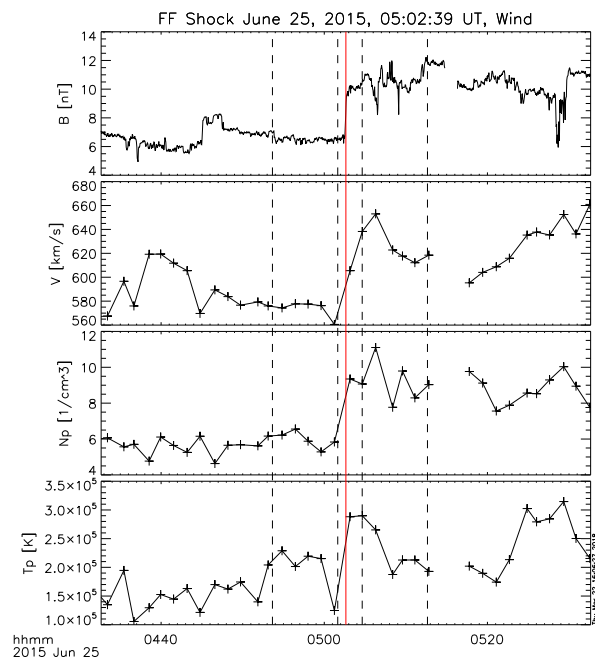
EUHFORIA is divided into two crucial sections. One approach is the Wang-Sheeley-Argge model (WSA), which incorporates magnetogram data to determine the plasma conditions at a distance of 0.1 AU. These conditions are necessary for predicting the background solar wind in the heliosphere (McGregor et al. , 2011; van der Holst et al. , 2010). Various magnetograms can be employed, such as the Global Oscillation Network Group (GONG; (Harvey et al. , 1996)) or the Helioseismic and Magnetic Imager (HMI) of the Solar Dynamics Observatory (SDO; (Schou et al. , 2012)). To begin with, in this model of the Sun's outer atmosphere, the three-dimensional magnetic field in the corona is determined by using a method called Potential Field Source Surface (PFSS) extrapolation, which was introduced by Altschuler & Newkirk (1969). Next, the magnetic field is stretched to a distance of 0.1 astronomical units (AU) utilizing the Schatten Current Sheet model as mentioned in (Schatten et al. , 1969). At the 0.1 AU limit, scientists determine the speed of the solar wind. Using this speed, they calculate the density and radial velocity at the outer boundary by employing empirical relationships (Pomoell & Poedts , 2018).

The next stage in EUHFORIA involves conducting a simulation that models the heliosphere, considering its 3D nature and also time-dependence. It is important to note that the thermodynamic and magnetic measurements were calculated using the coronal model during an MHD relaxation phase with a uniform grid, specifically within the range of 0.1 AU and 2 AU. **In particular**, a finite volume numerical method and a constrained transport scheme are used to solve the ideal MHD equations with a polytropic index of 1.5, ensuring that the solenoidal criteria are met (Pomoell & Poedts , 2018).

This research examined the development of eight specific CMEs between June 17 and June 29, 2015. Certain CMEs have distinct features: they are rapid, with speeds exceeding  $500km/s$ , and are not narrow, meaning their half-widths are greater than 35 degrees. The most crucial characteristic is that these selected CMEs are aimed at the Earth, with their source longitudes falling within a range of approximately plus or minus 60 degrees HEEQ. The Global Oscillation Network Group (GONG,Harvey et al. (1996)) introduced the solar wind at 00:03 UT on June 17, 2015. This information was randomly chosen

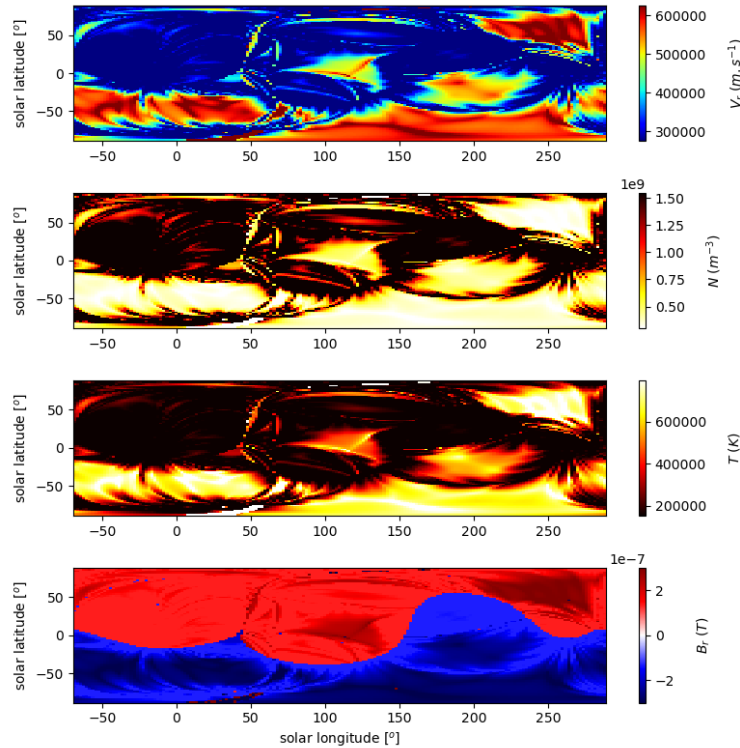


(a)



(b)

**Figure 5.** Fast forward (FF) shocks are demonstrated by OMNI and Wind spacecraft on 21 and 25 June 2015 that include total magnetic field  $B$ , the magnitude of the bulk velocity  $V$ , the proton density  $N_P$  and the proton temperature  $T_P$ . <http://ipshocks.fi/database>



(a)

**Figure 6.** The EUHFORIA input boundary condition that shows the distribution of the radial velocity ( $m/s$ ), number density ( $1/m^3$ ), temperature ( $K$ ) and radial magnetic field ( $T$ ).

to showcase the potential application of EUHFORIA.

155

GONG defines map products with 360 pixels in the east-west direction and 180 pixels in the north-south direction. Five different synoptic maps can be found in the GONG products. Two vital magnetogram synoptic maps are being created using data from the entire Carrington rotation. The complete magnetic field of the Sun is determined by utilizing accurately calibrated one-minute full-disk magnetograms from GONG's six regions.

160

Actually, the coronal model provides the required MHD input quantities at 21.5 Rs for the heliospheric solar wind module. The coronal module in EUHFORIA is data-driven and combines a PFSS magnetic field extrapolation from GONG or ADAPT magnetograms (1-2.5 Rs) with the semi-empirical Wand-Sheely-Arge (WSA) model and the Schatten current sheet (SCS) model to extend the velocity and magnetic field from 2.5Rs to 21.5 Rs. This is done with other semi-empirical formulas so that the density and temperature are also given at 21.5 Rs. EUHFORIA consists of two parts: a coronal domain and a heliospheric domain. The coronal part is a 3D semi-empirical model based on the WSA model, which provides the solar wind

165

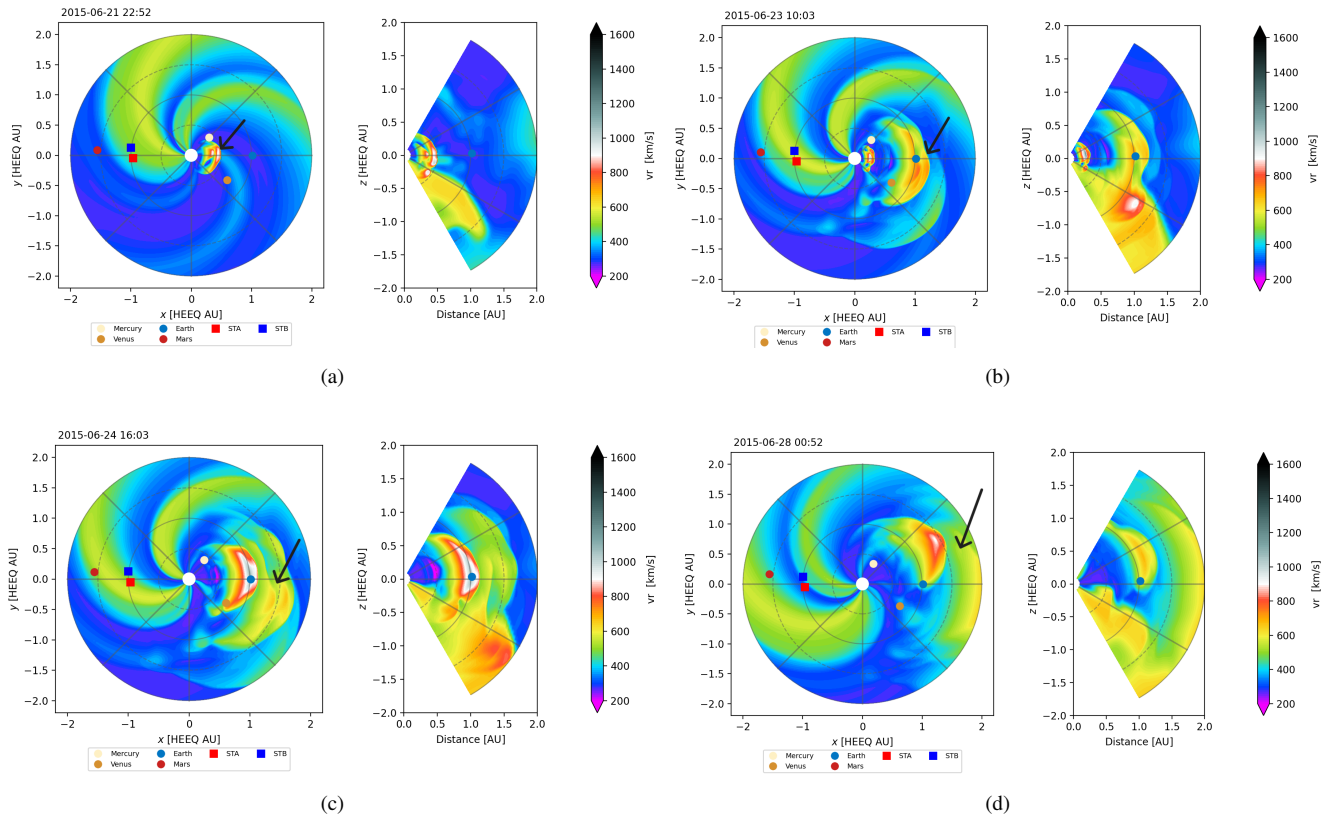


**Figure 7.** Snapshot of solar wind radial velocity ( $km/s$ ) from the MHD simulation with EUHFORIA. In each row, the left images depict the solution in the heliographic equatorial plane, and the right panels demonstrate the meridional plane that includes the Earth. CME1 was dedicated with the black arrow.

plasma conditions at the inner boundary of EUHFORIA at 0.1 AU. The photospheric magnetic field drives it via synoptic magnetogram maps. Then, Fig 6 is the heliosphere EUHFORIA boundary condition obtained by GONG map input and the coronal EUHFORIA calculations. Based on the significant disturbances in parameters, we can infer that the Sun is approaching  
 170 a period of maximum activity. Fig 6 displays the most recent prediction of the radial velocity, density, temperature, and radial magnetic field of solar wind.

The primary objective of this study was to assess the similarities and differences between observational data and the EUHFORIA simulation, a new space weather forecasting model for the inner heliosphere. EUHFORIA focuses on the characteristics of solar wind near the Sun and the transient events related to CMEs expanding into the heliosphere. The inputs of the model  
 175 include a corresponding file containing information about the magnetogram for the Corona model, as well as CMEs detected through observations from a coronagraph.

The part of EUHFORIA known as the heliosphere module focuses on studying the solar wind spanning 21.5 Rs to 2 AU (Po-moell & Poedts , 2018). A coronal module applies an input of 21.5 Rs. The text describes the process of expanding a system's radial velocity and magnetic field to a distance of 2 AU. The initial MHD solution is further altered by including a rotating inner boundary to relax the solar background wind. Consequently, there is a continuous flow of solar wind from 21.5 Rs to 2 AU in the co-rotating frame because the inner boundary condition remains unchanged and is only rotated. The equations are solved in the HEEQ frame, which is defined as the frame with its Z-axis directed in the rotation axis of the Sun, and its X-axis considered by the intersection of the solar equatorial plane and the solar central meridian of date that seen from the Earth.

185

Furthermore, when simulating the interaction between CMEs and solar wind topologies, it is often necessary to consider the surrounding ambient background and the ejecta itself, which typically includes an internal magnetic field. This ensures more accurate and realistic simulations instead of using a simpler hydrodynamic pulse. However, simulations involving magnetized ejecta can be computationally demanding when applied to Sun-to-Earth simulations (Jin et al. , 2017; Torok et al. , 2018). The velocity and density of the CMEs are associated with the dynamic pressure and also include signs of the moving of the interplanetary shock at the front of the CMEs. Because geomagnetic events can be caused by interplanetary shocks alone, the simplest models do not consider the internal magnetic field topology of the coronal mass ejection (CME)(Oliveria & Samsonov , 2018).

The EUHFORIA-heliosphere model can also simulate the launch of CMEs while considering the background solar wind. As a result, it can simulate CME evolution up to 2 AU and beyond. Most CMEs expand outward in a radial manner beyond the first few solar radii (Plunkett et al. , 1997). Because of the specific qualities observed in CMEs, the initial assumption about the cone-shaped halo-CMEs was modified by including additional parameters. These parameters determine the angle of the cone and the direction in which its central axis is oriented (Zhao et al. , 2002). They utilized uncharged variables to determine the angular breadth of the cone and the alignment of the cone's central axis. It is important to mention that the cone model was also utilized in the numerical simulation conducted by Odstrcil et al. (2004). The European Heliospheric Forecasting Information Asset (EUHFORIA) system completely validates the classic cone CME model.

Furthermore, considering the movement of CMEs, particularly in complex situations where there is interaction with the solar wind, poses a significant challenge for empirical approaches. Magnetohydrodynamic simulations provide a practical method to utilize physics-based modelling. The ENLIL model is the sole MHD lithospheric method utilized for forecasting, according to (Parsons et al. , 2011).

Despite the community's extensive effort to predict the arrival time of the CMEs, their accuracy remains uncertain. Both empirical and physics-based approaches have indicated that the root-mean-square error in predicting the arrival is 12 h and 10 h, respectively (Zhao & Dryer , 2014; Mays et al. , 2015). The primary concern is that different CMEs have varying levels of impact on Earth. Therefore, enhancing our capability to predict how these events will impact Earth is crucial. It is important

to highlight that the magnetic field of CMEs is crucial in determining their impact on Earth. Our ability to understand the characteristics of the magnetic field is very limited. Only recently have space weather directed methods related to predict the magnetic structure of CMEs been developed (Isavnin, , 2016; Kay et al. , 2017). The main difficulty for such empirical-based methods is to define the dynamics of the CME propagation, especially for complicated cases considering solar wind structures.

In this part, the outcomes of the EUHFORIA simulation for the inner heliosphere from 17 to 29 June 2015 are illustrated. The application includes the implementation of boundary conditions involving CMEs and solar wind. The study aims to examine the propagation of both CMEs.

Fig. 7 shows the representation of the heliospheric component of EUHFORIA, specifically focusing on the simulation of the underlying solar wind. The speed chosen is radial and matches the empirical speed recommendation. As depicted in Fig. 7, the size of the CME gradually increases as it travels. While the CME spreads, the thermal pressure causes it to expand consistently. The magnetic forces in the axial direction slow down the motion in the radial direction. CME magnetic pressure changes depending on the solar wind, causing the magnetic pressure to alternate between shrinking and expanding. The initial purely radial speed of the CME centre continues to propagate in the subsequent time step. The expansion of the CME is caused by two main forces: the Lorentz force and the drag force. The Lorentz force, denoted as  $J \times B$ , is equivalent to the multiplication of the current density ( $J$ ) and the magnetic field ( $B$ ). This force allows for the radial expansion of the CME (Sachdeva et al. , 2015). However, the drag force tends to impede the movement of the CME and is responsible for its gradual deceleration as it propagates (Chen & Kunkel , 2010; Subramanian et al. , 2012; Sachdeva et al. , 2017). The acceleration of the CME occurs when the Lorentz force becomes dominant over the drag force due to the shrinking and expanding of the magnetic field. Drag force can accelerate or decelerate depending on the relative speeds of the CME and the solar wind.

To effectively predict space weather, it is crucial to model the movement of CMEs in interplanetary space, considering the background solar wind. This approach ensures an accurate determination of the ejection's properties and enables the estimation of when the CMEs will reach Earth (MacNeice et al. , 2018; Reiss et al. , 2022). It should be noted that when simulating the arrival time, errors of approximately 1 day are commonly observed (Jian et al. , 2011; Gressl et al. , 2014). Despite this, many studies have focused on assessing how different models, including empirical/semi-empirical, machine learning, and MHD approaches, can account for the solar wind conditions in the surrounding environment (Barnard & Owens , 2022; Milosic et al. , 2023; Huang et al. , 2023).

We determine that CME1 will reach the Earth in approximately 46 hours. Based on the speeds projected in the CDAW catalogue (<https://cdaw.gsfc.nasa.gov/CME-list/>) CME1 has a linear fit speed of 1366.1 km/s, meaning it will take around 30.49 hours to reach the Earth. The second estimate is a rough approximation that does not consider the impact of drag or the interaction between CMEs as they travel towards Earth. These factors could explain the discrepancies observed. In the CME2 situation, this distinction becomes notable. The estimated arrival time of CME2 using EUHFORIA results is approximately

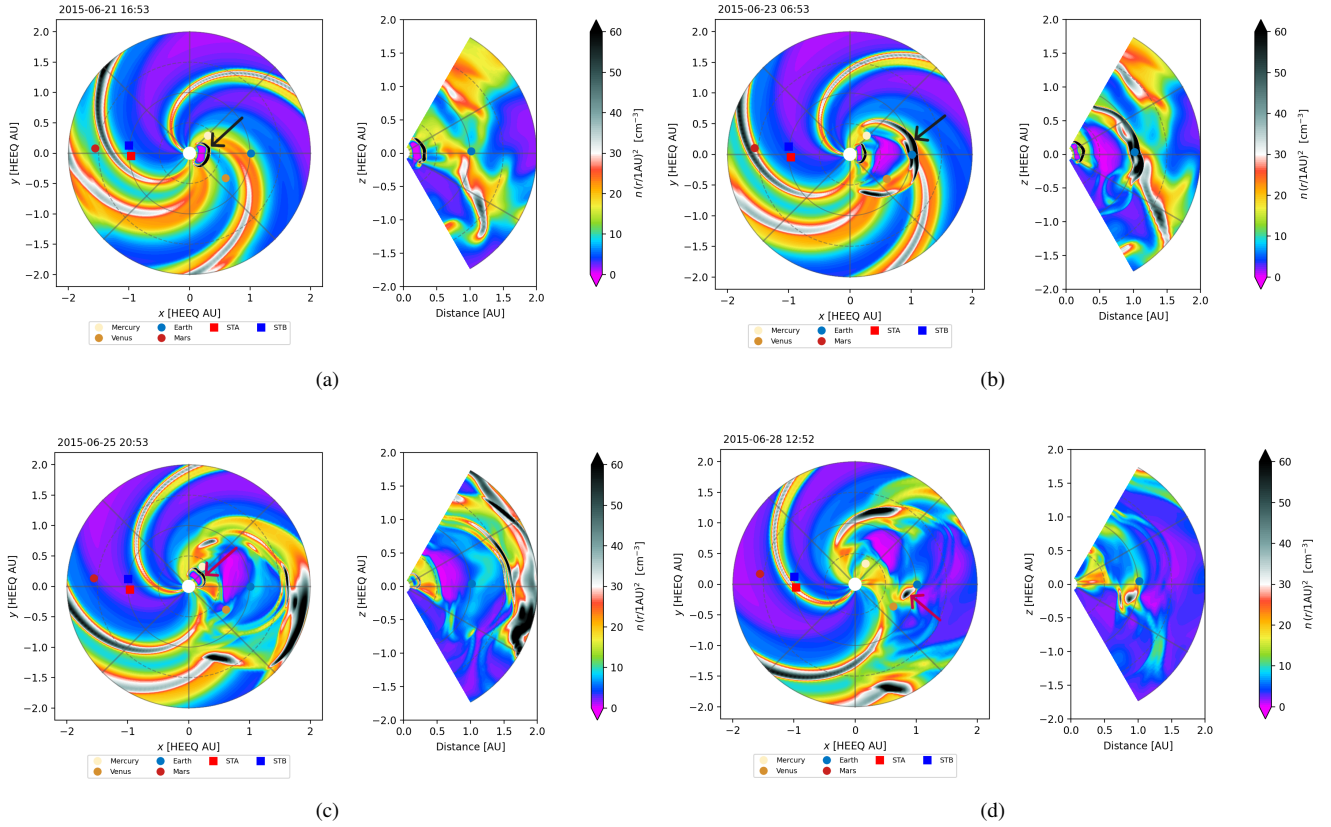


**Figure 8.** Snapshot of solar wind particle density ( $1/cm^{-3}$ ) from the MHD simulation with EUHFORIA. In each row, the left images depict the solution in the heliographic equatorial plane, and the right panels demonstrate the meridional plane that includes the Earth. CME1 was dedicated with the black arrow while CME2 was shown with the purple arrow.

70 hours, whereas using the linear fit speed of 1626.7 km/s, the estimated arrival time is around 26 hours. It can be inferred that how CMEs are launched is not particularly significant. Still, their interaction and movement in the heliosphere are the main factors determining their impact on Earth. Figs. 7 and 8 illustrate the growth of CME1 while it travels, while CME2 has diminished as it traveled, suggesting that CME2 has lost its energy. Afterwards, it was anticipated that a less powerful CME2 would reach its destination later than a stronger CME1, aligning with the calculated data.

Fig. 8 presents four snapshots of plasma density distribution. The following equation defines the plasma number density. Number density (in units of  $cm^{-3}$ ) scaled by  $r^2$  measured in astronomical units(AU).

$$n_{scaled} = n \frac{r^2}{1AU} . \quad (1)$$

In each plot, the left panel shows the amount in the heliographic equatorial plane, whereas the following panel displays the density in a meridional plane that includes Earth. In addition, the circles are shown with heliocentric radii set at values of  $r = 0.5, 1, 1.5, 2AU$ . It is important to mention that the inner planets' positions and the STEREO spacecraft's locations are indicated using markers. The information depicted in Fig. 8 indicates that the near-Earth environment experiences substantial changes in its dynamics caused by frequent eruptions. The panel (b) illustrates the arrival of CME1 at Earth, revealing that most of the CME reaches our planet. Panel (d) of Fig. 8 depicts the arrival of CME2 at the Earth's profile, demonstrating that only a section of CME2 reaches the Earth. Subsequently, it is anticipated that the first coronal mass ejection (CME1) will have more substantial repercussions on Earth when compared to CME2, which will be further elaborated on.

265

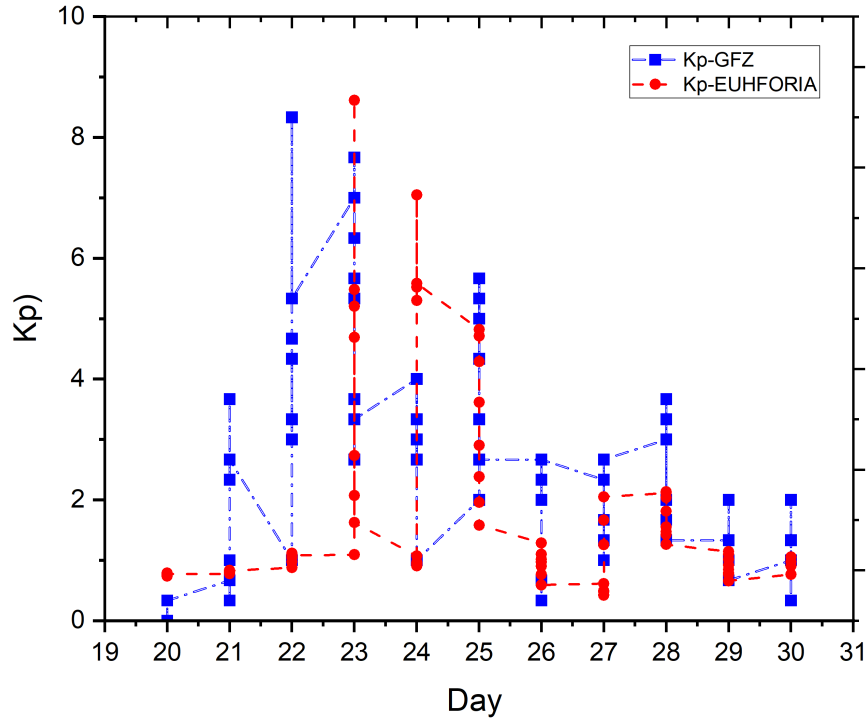
The study conducted by Burlaga & Ogilvie (1969) revealed that changes in the density of materials within the geomagnetic field caused stress rather than the occurrence of shocks. In addition, Rufenach et al. (1992) demonstrated that when solar wind dynamic pressure increases, there is typically a corresponding increase in the average magnetic field of the magnetosphere as measured by the GOES satellites in geosynchronous orbit. Due to the significant fluctuations in plasma density, it can be inferred that CME1 exerts greater pressure on the Earth's magnetosphere compared to CME2, which exhibits fewer plasma density fluctuations upon arrival.

The standardized K index of 13 magnetic observatories was used to derive the geomagnetic Kp index (Bartels & Veldkamp, 1950). This measurement assesses solar particle radiation by examining its magnetic reactions and determining the magnitude of geomagnetic storms. The K-index measures disruptions in the Earth's magnetic field in the horizontal direction and is assigned a value from 0 to 9. In calm situations, the Kp value is approximately 1, whereas during intense geomagnetic storms, it is roughly 9. The Kp index is a global measure of the K index, which is determined by analyzing data from magnetometers located on the ground (Bartels & Veldkamp, 1949). Indeed, regarding the reality of the situation, Kp serves as a remarkable gauge for abnormalities within the Earth's magnetic field. Presently, Kp holds significance as it quantifies the energy transfer from the solar wind to Earth and is employed by space weather services in almost real-time.

280

EUHFORIA utilizes a straightforward approach based on the empirical equation for linear prediction of Kp, originally proposed by Newell et al. (2008). **They not only investigate the values of Kp but considers ten different magnetospheric state variables, among which both the Kp and Dst indices. It investigates 32 coupling functions, of which twenty are viscously related, and twelve are merging related solar wind-magnetosphere coupling functions. The term coupling function is used because these functions couple the Kp index to the interplanetary conditions.** They discovered that the predictability of Kp can be greatly enhanced by incorporating both a merging factor and a viscous factor when analysing solar wind data. For instance, the solar wind information used for predicting the Kp index can be obtained by consulting the forecast outputs of EUHFORIA at Earth. The Kp index is computed by the model and presented as a time series. Fig 9 shows the changes in the Kp index over time, as calculated by EUHFORIA in panel (a) and defined by the GFZ research centre in panel (b). The results from the EUHFORIA numerical model align with the findings of the GFZ German research centre, demonstrating that the Kp index exhibits consistent changes over time. This implies that EUHFORIA can compute and potentially

290



(a)

**Figure 9.** Kp index calculated using synthetic EUHFORIA data at L1 (red) and determined by observational GFZ German research center (blue).

forecast the impact of CMEs on the Earth. The noteworthy aspect is that the previous findings demonstrating the significant role of CME1 in geoeffective outcomes align with the information presented in Fig 9. Due to the information presented in Fig 9, it can be observed that the  $K_p$  level is approximately 9 during the arrival of CME1. This signifies that CME1 leads to a severe geomagnetic storm. On the other hand, CME2 has a  $K_p$  value of around 3 during its arrival, indicating a moderate storm.

## 5 Conclusions

CMEs are responsible for causing significant geomagnetic storms and generating solar energetic particles (SEPs). Because of their significance in both science and society, studies on CMEs become highly important. Geomagnetic storms have the potential to generate particles in radiation belts, which can impact satellites, while SEPs can harm spacecraft. Consequently, it is crucial to examine the characteristics of CMEs, such as their movement and interaction, while being influenced by the

surrounding solar wind. Understanding their arrival time at Earth is imperative for accurately predicting space weather.

We utilized a numerical MHD model with three-dimensional time dependence to study expansive solar wind formations and  
305 explore the movement of certain CMEs and their propagation.

First, we examined a series of observational records that portrayed the situation. CMEs occurred on both June 21 and June  
25, 2015. Only two were chosen out of the various CMEs during that specific time. These two CMEs had distinct structures,  
one being a full halo CME and the other being a limb CME. It is important to mention that although they had similar speeds,  
310 other coronal mass ejections (CMEs) occurred around CME1. These interactions between the CMEs could have had a notable  
impact on Earth's magnetosphere and ionosphere.

Upon reviewing the observational data, we utilize the EUHFORIA simulation to differentiate the actions of both CME1  
and CME2. Using this simulation, we discovered how these CMEs move and the precise moment of their arrival at Earth's  
315 magnetosphere. Additionally, the geomagnetic parameter  $K_p$  was graphed and compared to the observed value to speculate  
which CMEs could lead to significant storms on Earth.

In conclusion, we have achieved the following key findings.:

- 320 1. In our research, we discovered that the "EUHFORIA" Heliosphere module, a three-dimensional MHD model, shows  
reasonably similar results to the WIND and OMNI observations including self-consistent structures.
2. It has been uncovered that as CMEs move through space, they gradually increase in size due to thermal pressure, the  
Lorentz force, and drag force.
- 325 3. Snapshots of the plasma density distribution illustrate that dominant part of the CME1 arrives at the Earth while, just  
flank of CME2 arrives the Earth. Additionally, CME1 generates notable plasma density pressures upon arrival, unlike  
CME2. Therefore, it is anticipated that the impact of CME1 on Earth will be much more significant than that of CME2.
4. The EUHFORIA model as well as observational data are utilized to calculate the arrival time of both CMEs at Earth.  
It was shown that there are significant discrepancies in the estimated arrival time of CME2 when computed using the  
two mentioned methods. It can be inferred that the initial traits of CMEs are not highly significant. Still, the interaction  
330 between CMEs and their movement through the heliosphere primarily influences their impact on Earth. This statement  
suggests that CME1 became stronger as it propagated, while CME2 became weaker. Consequently, it can be inferred  
that CME2 lost energy and reached Earth later.
5. The EUHFORIA numerical model's time variations of the Kp index coincided with the observational GFZ results. This  
states that EUHFORIA can accurately determine and possibly forecast the impact of CMEs on Earth. Furthermore, due to

335 the presence of several CMEs in the vicinity of CME1, this anticipated severe storm may be connected to the interaction of multiple CMEs.

We inferred that the solar wind in the background, which was identical in both CMEs, did not significantly impact the creation of magnetic storms. It can be inferred that the nature of CMEs, particularly their interaction with other CMEs, is the primary factor determining their geomagnetic impact on Earth.

340 *Code and data availability.* Observatory data used in this study was obtained from <http://ipshocks.fi/database>, <https://cdaw.gsfc.nasa.gov/CME-list>. This CME catalogue is generated and maintained at the CDAW Data Center by NASA and The Catholic University of America in cooperation with the Naval Research Laboratory. SOHO is a project of international cooperation between ESA and NASA. Besides, we used the EUHFORIA code for a numerical study that is publicly available via the VSWMC at <https://spaceweather.hpc.kuleuven.be/>.

*Author contributions.* Authors have contribution to write the manuscript.

345 *Competing interests.* The contributor author has declared that none of the authors has any competing interest.

*Acknowledgements.* For the computations, we used the infrastructure of the VSC–Flemish Supercomputer Center, funded by the Hercules Foundation and the Flemish Government-department EWI. SP is funded by the European Union. Views and opinions expressed are however those of the author(s) only and do not necessarily reflect those of the European Union or [name of the granting authority]. Neither the European Union nor the granting authority can be held responsible for them. This project (Open SESAME) has received funding under 350 the Horizon Europe programme (ERC-AdG agreement No 101141362). These results were also obtained in the framework of the projects C16/24/010 C1 project Internal Funds KU Leuven), G0B5823N and G002523N (WEAVE) (FWO-Vlaanderen), 4000145223 (SIDC Data Exploitation (SIDEX2), ESA Prodex), and Belspo project B2/191/P1/SWiM.

## References

- Altschuler, M. D., & Newkirk, G., 1969, *Solar Physics.*, 9, 131
- 355 Arge, C. N., Odstrcil, D., Pizzo, V. J., & Mayer, L. R., 2003, *AIP Conference Proceedings.*, 679, 190
- Barnard, L., & Owens, M., 2022, *Frontiers in Physics.*, 10, 1005621
- Bartels, J., & Veldkamp, J., 1950, *JGR.*, 55, 214
- Bartels, J., & Veldkamp, J., 1949, *JGR.*, 54, 295
- Bojan, V. 2021. *J. Space Weather Space Clim*, 11, 34
- 360 Brueckner, G. E., Howard, R. A., Koomen, M. J., Korendyke, C. M., & Eyles, C. J., et al. 1995, *Sol. Phys.*, 162, 357
- Burlaga, L. F., & Ogilvie, K. W., 1969, *J. Geophys. Res.*, 74, 2815
- Chen, J., & Kunkel, V., 2010, *The Astrophysical Journal.*, 717, 1105
- Cid, C., Cremades, H., & Aran, A., et al. 2012, *JGRA*, 117, A11102
- Dagnew, F. K. N., Gopalswamy, N., Tessema, S. B., Akiyama, S., & Yashiro, S., 2022, *APJ*, 903, 118
- 365 Dryer, M., 1994, *Space Sci Rev*, 6(3/4), 363
- Gieseler, J., Dresing, N., Palmroos, C., Von Forstner, J. L. F., & Veronig, A., et al., 2023, *Frontiers in Astronomy and Space Sciences*, 10, 3389
- Gopalswamy, N., Makela, P., Xie, H., & Yashiro, S., 2013, *SpWea*, 11, 661
- Gopalswamy, N., Makela, P., & Yashiro, S., 2018, *APJL*, 868, L19
- 370 Gopalswamy, N., Makela, P., & Yashiro, S., 2019b, *JPhCS*, 1332, 012004
- Gopalswamy, N., Akiyama, S., & Yashiro, S., 2020, *APJL*, 897, L1
- Green, LM., Torok, T., Vrsnak, B., Manchester, W., & Veronig, A., 2018, *Space Sci Rev*, 241, 46
- Gressl, C., Veronig, A. M., Temmer, M., Odstrcil, D., Linker, J. A., Mikic, Z., & Riley, P., 2014, *Solar Phys*, 289(5), 1783
- Harvey, J., Hill, F., & Hubbard, R., et al. 1996, *Science*, 271, 1284
- 375 Howard, R. A., Sheeley, N. R., Michels, D. S., & Koomen, M. J 1985, , 90, 8173
- Huang, Z., Toth, G., Sachdeva, N., Zhao, L., & Sokolov, I., et. al. 2023, *The Astrophysical Journal Letters*, 946(2), L47
- Isavnin, A. 2016, *Astrophys J.*, 833, 267
- Jin, M., Manchester, W.B., van der Holst, B., Sokolov, I., Toth, G., & Vourlidas, A., et al. 2017, *The Astrophysical Journal* , 834(2), 172
- Kay, C., Gopalswamy, N., Reinard, A., & Opher, M., 2017, *Astrophys J*, 835, 117
- 380 Jian, L. K., Russell, C. T., & Luhmann, J. G., 2011, *Solar Phys.*, 274(1-2), 321
- Kaiser, M. L., Kucera, T. A., Davila, J. M., St. Cyr, O. C., Guhathakurta, M., & Christian, E., 2008, *Space Sci. Rev.*, 136, 5
- Kilpua, E. K. J., Lumme, E., Andreeova, K., Isavnin, A., & Koskinen, H. E. J. 2015, *Journal of Geophysical Research (Space Physics).*, 120(6), 4112
- Kumar, P., Nakariakov, V. M., Karpen, J. T., & Cho, K. S. 2024, *Nature Communications.*, 15, 2667
- 385 Lavraud, B., & Rouillard, A., 2013, *Proc Int Astronom Union.*, 8, 273
- Lugaz, N., Farrugia, C.J., & Winslow, R.M., et al. 2016, *JGRA*, 121, 10861
- MacNeice, P., Jian, L. K., Antiochos, S. K., Arge, C. N., Bussy-Virat, C. D., & DeRosa, M. L., et al. 2018, *Space Weather*, 16(11), 1644
- Makela, P., Gopalswamy, N., & Yashiro, S., 2016, , 14, 368
- Manchester, W. B., Gombosi, IV. T. I., DeZeeuw, D. L., Sokolov, I. V., & Zurbuchen, T. H., et al., 2005, *Astrophys. J*, 622, 1225

- 390 Mays, M.L., Taktakishvili, A., Pulkkinen, A., MacNeice, P.J., & Rastter, L., et al. 2015, *Sol Phys*, 290, 1775  
 McGregor, S., Hughes, W., Arge, C., Owens, M., & Odstrcil, D., 2011, *Journal of Geophysical Research: Space Physics*, 116  
 McLaughlin, J. A., & Nakariakov, M. V., Dominique, M., Jelínek, P., & Takasao, S. 2018, *SSRv*, 214, 45  
 Michalek, G., Gopalswamy, N., & Yashiro, S., 2019, *APJ*, 880, 51  
 Milosic, D., Temmer, M., Heinemann, S. G., & Vrsnak, B., et al. 2023, *Solar Physics*, 298(3), 45
- 395 Newell, P. T., Sotirelis, T., Liou, K., & Rich, F. J. 2008, *J. Geophys. Res: Space Phys*, 113, A04218  
 Nindos, A., Patsourakos, S., Vourlidas, A., Cheng, X., & Zhang, J. 2020, *Astron Astrophys*, 642, A109  
 Odstrcil, D., Linker, J. A., Lionello, R., Mikic, Z., Riley, P., Pizzo V. J., & Luhmann, J. G., 2002a, *J. Geophys. Res*, 107(A12), 1493  
 Odstrcil, D., Pizzo, V. J., Linker, J. A., Riley, P., Lionello, R., & Mikic, Z., 2004a, *J. Atmos. Sol. Terr. Phys*, 66, 1311  
 Odstrcil, D., Riley, P., & Zhao, X.P., 2004b, *J. Geophys. Res. Space. Phys*, 109
- 400 Oliveria, D. M., & Samsonov, A. A., 2018, *AdSpR.*, 61, 1  
 Parsons, A., Biesecker, D., Odstrcil, D., Millward, G., Hill, S., & Pizzo, V., 2011, *Space Weather* , 9  
 Pirjola, R. 2005, *AdSpR.*, 36, 2231  
 Plunkett, S. P., et al. 1997, *Sol.Phys.* , 175, 699  
 Pomoell, J., & Poedts, S., 2018, *Journal of Space Weather and Space Climate.*, 8, A35
- 405 Poedts, S., Kochanov, A., Lani, A., et al. 2020, *Journal of Space Weather and Space Climate.* , 10, 14  
 Pulkkinen, T. 2007, *LRSP.*, 4, 1  
 Reiss, M. A., Muglach, K., Mullinix, R., Kuznetsova, M. M., Wiegand, C., & Temmer, M., et al. 2022, *Advances in Space Research.*, in press  
 Rville, V., Brun, A. S., Matt, S. P., Strugarek, A., & Pinto, R. F., 2015, *APJ.* , 798, 116  
 Riley, P., & Ben-Nun, M., 2021, *Space Weather.*, 19(6), e02775
- 410 Rufenach, C. L., McPherron, R. L., & Schaper, J. 1992, *J. Geophys. Res*, 97, 25  
 Sabri, S., Vashghani Farahani, S., Ebadi, H., Hosseinpour. M., & Fazel, Z 2018, , 479, 4991  
 Sabri, S., Vashghani Farahani, S., Ebadi, H., Hosseinpour. M., & Fazel, Z 2018, *MNRAS*, 479, 4991  
 Sabri, S., Poedts, S., & Ebadi, H. 2019, *A & A*, 623, A81  
 Sabri, S., Ebadi, H., & Poedts, S. 2020, *APJ.*, 902, 11
- 415 Sabri, S., Vashghani Farahani, S., Ebadi, H., & Poedts, S. 2020, *Sci Rep*, 10, 15603  
 Sabri, S., Ebadi, H., & Poedts, S. 2021, *Apj*, 922, 123  
 Sabri, S., Ebadi, H., & Poedts, S. 2021, *Apj*, 924, 126  
 Sabri, S., Ebadi, H., & Poedts, S. 2022, *Apj*, 924, 126  
 Sabri, S., Ebadi, H. & Poedts, S. 2023, *Apj.*, 944, 72
- 420 Sachdeva, N., Subramanian, P., Colaninno, R., & Vourlidas, A., 2015, *The Astrophysical Journal*, 809, 158  
 Sachdeva, N., Subramanian, P., Vourlidas, A., & Bothmer, V., 2017, *Solar Physics*, 292, 1  
 Samara, E., Pinto, R. F., & Magdalenic, J., et al. 2021, *A & A*, 648, A35  
 Schatten, K. H., Wilcox, J. M., & Ness, N. F. 1969, *Solar Physics*, 6, 442  
 Schmieder, B., Aulanier, G., & Vrsnak, B. 2015, *Solar Physics*, 290, 3457
- 425 Schou, J., Borrero, J., & Norton, A., et al. 2012, *The Solar Dynamics Observatory*, 327  
 Scolini, C., Messerotti, M., Poedts, S., & Rodriguez, L. 2018, *JSWSC*, 8, A9  
 Song, H.Q., Zhang, J., Chen, Y., & Cheng, X. 2014, *Astrophys J Lett*, 792(2), L40

- Subramanian, P., Lara, A., & Borgazzi, A. 2012, *Geophysical research letters*, 39
- Torok, T., & Kliem, B. 2005, *ApJ*, 630, L97
- 430 Torok, T., Downs, C., Linker, J.A., Lionello, R., Titov, V.S., & Mikic, Z., et al., 2018, *The Astrophysical Journal*, 856(1), 75
- van der Holst, B., Manchester, W., & Frazin, R., et al., 2010, *apj*, 725, 1373
- Verbeke, C., Mays, M. L., Kay, C., Riley, P., Palmerio, E., & Hinterreiter, J., et al., 2022, *Advances in Space Research*, 8, A9
- Wu, S. T., Guo, W. P., Michels, D. J., & Burlaga, L. F., 1999, *J. Geophys. Res.*, 104(A7), 14,789
- Zhao, X. P., Plunkett, S. P., & Liu, W., 2002, *J. Geophys. Res.*, 107(A8), 1223
- 435 Zhao, X. P., & Webb, D. F., 2003, *JGRA.*, 108, 1234
- Zhao, X., & Dryer, M., 2014, *Space weather.*, 12, 448
- Zheng, Y. 2013, *Space Weather.*, 11, 641